# FPGA-Based Reconfigurable Processor for Ultrafast Interlaced Ultrasound and Photoacoustic Imaging

**Umar Alqasemi**,
Biomedical Engineering Program, University of Connecticut, Storrs, CT

**Hai Li**,
Electrical and Computer Engineering Department, University of Connecticut, Storrs, CT

**Andrés Aguirre [Member, IEEE]**, and
Electrical and Computer Engineering Department, University of Connecticut, Storrs, CT

**Quing Zhu [Senior Member, IEEE]**
Biomedical Engineering Program, University of Connecticut, Storrs, CT

Electrical and Computer Engineering Department, University of Connecticut, Storrs, CT

Quing Zhu: zhu@engr.uconn.edu

## Abstract

In this paper, we report, to the best of our knowledge, a unique field-programmable gate array (FPGA)-based reconfigurable processor for real-time interlaced co-registered ultrasound and photoacoustic imaging and its application in imaging tumor dynamic response. The FPGA is used to control, acquire, store, delay-and-sum, and transfer the data for real-time co-registered imaging. The FPGA controls the ultrasound transmission and ultrasound and photoacoustic data acquisition process of a customized 16-channel module that contains all of the necessary analog and digital circuits. The 16-channel module is one of multiple modules plugged into a motherboard; their beamformed outputs are made available for a digital signal processor (DSP) to access using an external memory interface (EMIF). The FPGA performs a key role through ultrafast reconfiguration and adaptation of its structure to allow real-time switching between the two imaging modes, including transmission control, laser synchronization, internal memory structure, beamforming, and EMIF structure and memory size. It performs another role by parallel accessing of internal memories and multi-thread processing to reduce the transfer of data and the processing load on the DSP. Furthermore, because the laser will be pulsing even during ultrasound pulse-echo acquisition, the FPGA ensures that the laser pulses are far enough from the pulse-echo acquisitions by appropriate time-division multiplexing (TDM). A co-registered ultrasound and photoacoustic imaging system consisting of four FPGA modules (64-channels) is constructed, and its performance is demonstrated using phantom targets and *in vivo* mouse tumor models.

## I. Introduction

Photoacoustic tomography (PAT) is an emerging imaging modality that combines excellent optical absorption contrast, comparable to the other optical imaging techniques, with good ultrasound (US) resolution [1]. Optical absorption of biological tissue in the near-infrared region (NIR) is directly related to its blood hemoglobin content, which is the summation of oxygenated and deoxygenated hemoglobin concentrations. Abnormal growth of tumor cells requires a greater supply of nutrients and oxygen than normal tissue, which triggers rapid growth of a complex blood vessel network or tumor angiogenesis. Tumor angiogenesis is a functional marker of tumor progression and metastasis. Thus, PAT is an excellent tool to image tumor angiogenesis development as well as tumor oxygenation when multiple optical wavelengths are utilized. The penetration depth of PAT is scalable with the central frequency and bandwidth of the ultrasound transducer as long as adequate light fluence can be delivered to the targets [1]. However, PAT images do not show optically non-absorbing structures of the tissue, which makes it difficult to correlate the absorption contrast with anatomical structures. Ultrasound, on the other hand, provides excellent anatomical structure information related to tissue acoustic impedance but lacks functional contrast in diagnosing early stage cancers [2]. Combining the two modalities is a logical extension of each modality alone because both use the same ultrasound detection frontend, and, more importantly, the combined modality provides complimentary information of tumor vasculature and tumor morphology, which are valuable for cancer detection and diagnosis as well as detection and diagnosis of other diseases [3]–[7]. Furthermore, the structural information provided by ultrasound imaging can be employed to improve the PAT image quality by incorporating more accurate models for acoustic propagation in PAT reconstruction [8]–[10].

The first system of combined ultrasound and photoacoustic imaging was implemented by Niederhauser *et al.* in 2005 for vascular imaging; they reported the ability to alternately acquire and display the dual modality images side by side but not in a real-time interlaced scheme [11]. Another combined system for intravascular imaging was introduced by Sethuraman *et al.* in 2006, however, the data processing for co-registering the two modality images was done off-line [12]. Our group developed a co-registered ultrasound and photoacoustic 3-D imager in 2007, but the data acquisition speed was very low [6], [13]. In 2008, Kolkman *et al.* modified a commercial ultrasound unit to perform combined ultrasound and photoacoustic imaging; however, because they used the same commercial frontend of hardware-based delay-and-sum beamformer, it required a high laser pulse repetition rate (PRR) of 1 kHz, which made the laser radiation exceed the maximum permitted exposure by the International Electrotechnical Commission (IEC). Moreover, they obtained good frame rate in each modality alone, but the co-registration is not done in a real-time interlaced scheme [14]. Ermilov *et al.*, developed two laser optoacoustic imaging systems in 2009; one of them could work in both optoacoustic and ultrasound modes. However, this system required switching between optoacoustic and ultrasound data acquisition from a separate optoacoustic machine and a commercial ultrasound scanner, and real-time co-registration of the two images wasn't achieved [15]. Harrison *et al.* developed a real-time combined ultrasound and photoacoustic microscopy system in 2009 that interlaced

the ultrasound and laser pulses for co-registered imaging. The system used a single mechanically scanned high-frequency ultrasound transducer with a unique light delivery probe to scan thin-tissue samples [16].

In this paper, we present a unique field-programmable gate array (FPGA)-based reconfigurable processor that allows real-time switching and interlacing between the two imaging modalities (i.e., ultrasound and photoacoustic imaging) in one machine and the same receiving frontend. The system features a modular design and the ability of real-time parallel acquisition from 64 channels, with each channel sampled at 40 MHz. The FPGA processor is responsible for controlling the hardware, acquiring the digital data from the analog-to-digital converters, parallel data storing and processing, beamforming, and communication with a DSP coordinator to transfer data to a host PC [17]. Each modality requires different considerations (e.g., different storage sizes, different beamforming algorithms, etc.), which is the driving need for a reconfigurable processor to switch between the two modalities in real-time using the same receiving frontend, and to manage the digital resources for optimizing the speed in each mode. Furthermore, the FPGA code allows real-time acquisition of pre-beamformed data for both modalities [18], this capability will provide researchers with an extended tool for forming their own images using extended imaging algorithms. Though the overall achieved co-registered frame rate is 1 Hz, this is primarily because of the use of the current DSP board, which has a slow link to the host PC. This part of the system is readily upgraded with a high-speed DSP board.

In this article, the system architecture is explained in detail, especially the digital design and structure of the reconfigurable FPGA-based processor [19]. Phantom testing of an ink tube is used to demonstrate the real-time capability of the system and the complimentary information that both modalities can provide. *In vivo* experiments of a mouse tumor injected with the absorption contrast agent indocyanine green (ICG) have demonstrated the potential application of our co-registered ultrasound and photoacoustic imager in monitoring the dynamic response of the tumor.

## II. System Description

### A. Block Diagram

The overall block diagram of the system is shown in Fig. 1. The system has a modular design that allows the number of channels to be easily upgraded as required in multiples of 16 channels. Each module consists of five boards grouped together: a customized E-shaped board for 16-channel ultrasound transmission and reception (preamplification), and two commercial ultrasound 8-channel receiving boards connected through a customized adaptor board to a commercial FPGA digital data-capturing board (HSC-ADC-EVALCZ). The commercial ultrasound receiving boards contain a microchip (AD9272-65EBZ, Analog Devices Inc., Norwood, MA) [20], which has a programmable octal low-noise amplifier (LNA), variable gain amplifier (VGA), anti-aliasing filter (AAF), and analog-to-digital converter (ADC) with 40 MHz sampling frequency. The FPGA board contains a Virtex-4 Xilinx FPGA (Xilinx Inc., San Jose, CA), and a USB interface that allows interfacing with the receiving boards' microchips through a serial programming interface (SPI) link that controls the characteristics of the chip (e.g., gain, bandwidth, etc.). Also, the FPGA captures

the octal low-voltage differential signals (LVDS) of double data rate (DDR) transferring at 240 MHz from each receiving board. The block diagram of the 16-channel module is shown in Fig. 2 [21], [22].

The modules are plugged into a motherboard that fans out the channels from all the modules to the ultrasound connector. The motherboard also serves as a common power supply and ground plane to all the modules. Each module is also connected through three ribbon cable assemblies to another adaptor board to allow a digital signal processor (DSP) board (TMS320C6455 DSK Module, Spectrum Digital Inc., Stafford, TX) to communicate back and forth with all the modules' FPGAs. Hence, the DSP board serves as a central coordinator between the modules, and it performs the necessary communication with the personal computer and user interface.

A Ti:sapphire (LS-2134, Symphotics TII Corp., Camarillo, CA) laser optically pumped with a Q-switched Nd:YAG laser (LS-2122, Symphotics-TII) delivers 12-ns pulses at 15 Hz with a wavelength tunable from 700 to 950 nm [23]. The laser beam is diverged with a planoconcave lens and homogenized by a circular profile engineered diffuser (ED1-S20, ThorLabs Inc., Newton, NJ) to produce a uniform approximately 20-mm-diameter illumination at the sample [23], [24].

## B. Overall Scheme of Co-Registered Acquisition

To initiate the acquisition process, a user interface control developed in Visual C++ is started first. The software calculates the delay coefficients for pulse-echo (PE) transmission, and the PE and photoacoustic (PA) dynamic focusing delay coefficients for beamforming, which is based on the user-selected transducer and its parameters and on the scan type (i.e., sector, linear, or quasilinear scan). After that, the PE delay coefficients are downloaded to the DSP board, which distributes them to the FPGAs of each module based on their attached channel order. The PE beamforming is done simultaneously in the FPGA of each module from its local 16 channel RF data to reduce the amount of data to be transferred to the DSP, where the sub-beam lines formed from different modules are summed up and transferred to the PC. On the other hand, for PA, the averaged RF data of each channel is transferred to the PC where the beamforming is done [2], [25].

Once the delay coefficients are transferred to the FPGAs, the DSP triggers all of the FPGAs to enable the transmission (Tx) FIFOs[1], and simultaneously starts filling the US receiving (Rx) FIFOs for acquiring PE A-lines (i.e., A-mode scan) until all the A-lines for forming an image frame are acquired. After that, it waits for the synchronization pulse from the laser to start filling the Rx FIFOs again until the required imaging depth is covered, and this process is repeated for *N* averaging times while the RF data of the channels are transferred instantly to the DSP and accumulated. Once the DSP receives all of the PE and PA data, the whole data thread for an image frame will be transferred to the PC using a local area network (LAN) interface. Next, the PC will do PA beamforming, PA and PE envelope detection, and scan conversion. Finally, the dual-modality images will be co-registered and displayed in a single frame with different color scales [2], [17], [25].

---

[1]First-in first-out, a type of memory that pumps out its values serially at the rising edge of the synchronizing clock.

Thus, the FPGA serves as a 16-channel processing unit that controls transmission, data acquisition from the receiving boards' ADCs, interfacing with the laser unit, preprocessing of the RF data, and 16-channel dynamic focusing of pulse-echo A-lines. Therefore, it is important that the FPGA code is properly designed to be reconfigurable to re-optimize the speed and usage of the available resources in each imaging mode.

## III. FPGA Code Structure

### A. Block Diagram

The overall block diagram of the FPGA code is shown in Fig. 3. The code was written in Verilog hardware description language (HDL). It consists of a 16-channel LVDS DDR capture code that converts the ADC 240-MHz serial outputs to single-ended parallel outputs at 40 MHz (i.e., the sampling frequency). The RF data are preprocessed and then stored in a dual-port RAM block. The master controller manages the overall flow of the data and provides the reconfigurability of the code, which is eventually controlled by a few DSP control signals [19], [26]–[31].

The LVDS DDR ADC outputs are decoded to parallel single-ended outputs at 40 MHz. After that, the data stream is preprocessed and stored in the Rx FIFO/RAM when the appropriate control signals are received from the master controller. The master controller makes its decisions based on the laser synchronization and DSP control signals to control the Rx and Tx FIFOs, to enable/disable beamforming, and to change the DSP EMIF structure and memory size for reading and writing. The function of the main blocks is summarized in the remainder of this section.

### B. Preprocessing and Rx FIFO Storage

The RF data are preprocessed immediately before being stored in the dual I/O RAM blocks. The preprocessing includes digital filtering and bias cancellation. The dual-port RAM block used for storage is RAMB16, which has 2 kB of memory if used as a dual-port RAM block [28]. Several RAMB16 blocks are lumped together to form a RAM with more storage memory. The outputs from the ADCs are 12-bit quantized; and the length of each Rx FIFO is 4096; which corresponds to a depth of penetration ($d_p$) calculated as

$$d_p = 4096 \times (0.15 \, \text{cm}/\mu\text{s}) / 40 \, \text{MHz} = 15.36 \, \text{cm},$$

where the speed of sound is assumed to be 0.15 cm/μs. Note that this is for one-way travel of the ultrasound wave; however, for PE, 4096 FIFO length corresponds to half that distance, which is 7.68 cm. On the other hand, to form a co-registered frame, it's necessary that both images from PA and PE have the same depth. Thus, for PA, only the first 2048 values of the FIFOs are considered, whereas all 4096 of the values are considered for PE. The Rx FIFO/RAM used for that purpose is shown in Fig. 4 [2], [25], [26].

The ADC RF data are stored automatically at each rising edge of the sampling clock to the FIFO port, whereas these values can be randomly accessed with a reading address given by the DSP EMIF or the beamformer from the RAM port. The FIFO is made by generating the

address automatically at each clock rising edge with a digital counter for the FIFO port of the dual-port RAM. The transmission (Tx) RAM/FIFO has similar structure but the reading and writing ports are reversed to allow feeding then transmitting.

## C. DSP EMIF Interface and Control

The DSP external memory interface (EMIF) includes the necessary scheme to communicate with the DSP board. The DSP address, data bus, and basic read/write control signals are connected with one 80-pin connector to each FPGA.

The other DSP control signals are connected through two 40-pin connectors. Some of these signals are used for communicating with FPGAs based on the mode of imaging, acquisition and transmission, and reset. Also, some of the signals are used to inform the DSP about the laser pulse synchronization, the change of the wavelength of the laser, and whether the beamforming RAM is ready from the FPGAs. The DSP EMIF data bus and address lines are also connected to the master controller, which decides where to connect them based on the mode of imaging by digital multiplexers.

In PE mode, the DSP writes the beamforming delay coefficients of 1024 focusing points distributed over 7.68 cm depth. The value of the coefficient is basically the address of each channel to be accessed in the Rx FIFO/RAM for each focusing point. The DSP also writes the Tx FIFO binary values for a length of 1024 to be transmitted out at 100 MHz clock speed [2], [30]. After the beamforming is done, the DSP reads the beam-line output from the beamforming RAM. In PA mode, the DSP only reads the RF data directly from the Rx FIFOs, where only the first 2048 values from each channel Rx FIFO/RAM are accessed.

## D. Multi-Thread Ultrasound Beamformer

The delay-and-sum beamforming of the pulse-echo acquired RF data are done within the FPGA for the local 16 channels. The method of our beamforming is similar to [17], except that we use only coarse delay coefficients because our ADC sampling frequency is reasonable compared with the transducer frequency. In addition, we directly access the value of the RF data from the Rx FIFO with the required delay corresponding to a linear function of the address (e.g., 3000 address value at 40 MHz sampling frequency corresponds to $3000/40$ MHz $= 75$ μs delay). This address is precalculated in the PC and then transferred to the DSP, which feeds it to each FPGA at the beginning of each A-line acquisition [2], [28]. The beamformer code iteratively accesses the Rx FIFO/RAM of each channel for each focusing point with the corresponding precalculated address; and then sums all of the accessed values and stores them in the beamformed data RAM. However, because we want the beamformer output to have the same length of the Rx FIFO (4096), 3072 more points are added between the 1024 focusing points by interpolation. The beamformer performs the fetching of addresses for different channels and interpolates the three other points between each pair of focusing points in an overlapping fashion to reduce the total time needed. Forty-four steps are required to calculate the value of the beam at a certain focusing point and its three neighboring points; they are repeated 1024 times. With a 50-MHz processing clock, we achieve $44 \times 1024/50$ MHz $= 901$ μs per beam-line. If 100 beam-lines per frame are used, it's 90 ms per frame. If higher speed is needed, a 100 MHz processing clock can be used,

and 45 ms per frame can be achieved, which corresponds to a maximum frame rate of 22 fps. If more speed is needed, it's also possible to truncate the three points in between each two focusing points, that will shrink the number of steps down to 20 and provide more than 60 fps maximum frame rate (no other delay factors considered in this calculation) [2].

The other three points between each two focusing points are calculated by interpolating addresses between the two focusing points' addresses as follows:

$$A_{\text{inc}} = (A_4 - A_0)/4$$
$$A_1 = A_0 + A_{\text{inc}}$$
$$A_2 = A_1 + A_{\text{inc}}$$
$$A_3 = A_2 + A_{\text{inc}},$$

where $A_{\text{inc}}$ is the address increment step between the points, $A_0$ is the preceding focusing point address, $A_4$ is the next focusing point address, $A_1$ is the first interpolated point address, $A_2$ is the second interpolated point address, and $A_3$ is the third interpolated point address between the two focusing points [32].

The beamformer does 1024 iterations, each of 44 steps (6-bit counter). Thus, four beamformed data points are stored at the end of each iteration. After finishing 1024 (10-bit counter) iterations, the total number of stored beam points is 4096 in the beamformed data RAM and a beamforming ready flag is raised. The DSP starts reading the beamformed data RAM once it receives the flag. The block diagram of the multi-thread beamformer is summarized in Fig. 5.

The beamforming is done in pulse-echo mode only to reduce the amount of data to be transferred from each FPGA board by a factor of 1/16 for each beam-line; this is not done for PA mode because there is much less data to transfer. However, it would be easy to extend the idea of the pulse-echo beamformer to PA mode, and to have both of them done using the same FPGA code if higher PA processing speed is needed.

### E. Master Controller and Reconfigurability

Most of the interconnects between different blocks are controlled by the master controller, which is eventually controlled by the DSP control signals. The master controller tries to organize both imaging processes in a very accurate manner using the precise timing and control capabilities of the FPGA.

Based on the DSP signal for the mode of imaging, the master controller restructures the functions of the FPGA and its storage handling. In PA mode, the Rx FIFO/RAM length is reduced to 2048 and the output of the Tx RAM/FIFO is disabled and replaced by zero value. The FPGA triggers the DSP by an elongated laser synchronizing pulse and makes sure that it receives the trigger by handshaking. Then, the Rx RAMs for 16 channels are lumped together and made directly accessible by the DSP board as one RAM.

On the other hand, in PE mode, the Tx RAM/FIFO, beamformer, and the beamformed data RAM are enabled. The DSP triggers the FPGA after writing to the Tx RAM/FIFO and the

beamforming coefficients RAM to start A-line acquisitions. Time-division multiplexing (TDM) is done to allow acquisition of the PE data while the laser is still pulsing. The master controller checks the laser synchronization pulse and how far it is from the DSP trigger. If the laser pulse is more than 0.2 ms (4096/40 MHz) away (to ensure that the generated photoacoustic signal from the running laser is not interfering with the pulse-echo signals), the master controller starts shifting out the values of the Tx FIFO and at the same time storing the received RF data to the Rx FIFOs. Otherwise, it will wait to ensure that the required delay is achieved. If, by coincidence, the acquisition is started but the laser pulse comes before the acquisition is finished, the master controller will reset the Rx storage and restart the acquisition once the laser pulse is at least 0.2 ms away. Fig. 6 shows the block diagram of the TDM scheme.

Note that the TDM scheme is important because the Nd:Yag laser pump is self-triggering at 15 pulses/s and its manufacturer doesn't guarantee stable output pulse energy if an external trigger is used with a lower pulse repetition rate (because, in that case, the pulsing must be shut off during PE acquisition). It would also be more difficult to electro-optically shut off the laser output than using the TDM scheme. Note also that if the PE signal contrast is very high, the PA interference won't be noticed without the TDM. Nevertheless, if the PA target contrast is very high and the PE contrast is very low, the PA interference will definitely show up randomly in the PE image when the PE acquisition is done close to the laser pulse. However, with the TDM scheme, it is guaranteed that the PA interference won't interfere with the PE acquisition.

## IV. Results

### A. Phantom Experiment of Ink Tube

To demonstrate the real-time imaging capability of our co-registration system, we imaged a polyethylene tubing with a 0.58 mm inner diameter fixed to a plastic frame forming three parallel segments with a separation of approximately 1 cm, as shown in Fig. 7.

A 1.3-MHz 64-channel phased-array ultrasound transducer was placed facing the open side of the frame. Both the frame and the transducer were immersed in a calibrated intralipid solution of $0.03$ cm$^{-1}$ absorption coefficient and $6$ cm$^{-1}$ reduced scattering coefficient at a depth of 1 cm, where the laser beam was expanded over the tubing area, as shown in Fig. 7. The calibration was performed using a diffused optical system [33]. Initially, the tubing was empty and only the ultrasound image (gray scale) showed acoustic contrast. At this point the photoacoustic image (color scale) showed no contrast because the tubing was almost transparent to light. Next, a black Indian ink was injected into the tubing, as shown in Fig. 8, and the superimposed photoacoustic images revealed local optical contrast of each segment, one by one, as more ink was injected ( 🎞️ ). The system gain was set to 50 dB, and the PE parts (gray color scale) of the images were normalized to the maximum of PE beams with 20 dB dynamic range for display, whereas the PA parts (red-yellow color scale) were normalized to a constant value, which corresponded to the peak of the PA beams when the ink was in, with 40 dB dynamic range. Note that, for this experiment, the photoacoustic signal was averaged 7 times with the 15-Hz laser tuned at a wavelength of 740 nm; the achieved speed with this number of averages is around 0.5 co-registered frames/s.

## B. Mouse Experiment with Dynamics of ICG Injection

The *in vivo* imaging capability of our imager is demonstrated using a mouse tumor model grown in the right mammary pad. A water bath was placed between the tumor and the ultrasound transducer as a coupling medium. The laser beam illuminated the tumor through the coupling medium from one side of the ultrasound transducer, as shown in Fig. 9. The system gain was also set to 50 dB, and both PE and PA parts of the images were normalized to their own peaks with 40 dB dynamic range. All experiments were performed under anesthesia by the inhalation of 1.5% to 2% isoflurane. The animal protocol was approved by the Institutional Animal Care and Use Committee of University of Connecticut. Two sets of experiments were performed.

In the first set of experiments, tumor uptake and dye wash out time was monitored for about 80 min after injection of ICG, which is an optical contrast agent. The dye concentration is 100 μM, and the illumination was done at 740 nm, which matches the peak absorption of the dye [34]. In about 5 to 6 min, the maximum photoacoustic signal in the tumor area was increased by about 70 to 80% and areas of the tumor showed more filling. Fig. 10 shows the normalized maximum photoacoustic signal, which is normalized to the maximum PA signal just before the injection, from the tumor area. The maximum PA signal gradually increased in the first 3.5 min after injecting ICG, after that, it started to wash out slowly from the blood stream. The fluctuations in the PA signal are likely due to the cardiovascular dynamics of the mouse. Furthermore, Fig. 11 shows how the area of the tumor is more filled with the photoacoustic contrast 3.5 min after injection compared with the image before injection. It is noted that the laser pulse energy was monitored during the imaging process to compensate for the drift of the laser energy per pulse [35]. The compensation was done by adding a transparent flat piece of glass in the path of the laser beam at about 30° angle of incidence, which reflected a small fixed percentage of the laser light beam to an energy meter. The energy meter output was recorded and precalibrated with phantom experiments such that the peak PAT signal is proportional to the energy of the laser pulse (with ± 10% maximum uncertainty over 2 h period), and then synchronized with the PC acquisition software. Note also that the mouse temperature was assumed to be constant because a heating pad was used throughout the experiment to help the animal regulate its body temperature [36].

In the second set of experiments, the wavelength of the laser was manually scanned from 705 to 835 nm during a 30-s *in vivo* imaging session. Shown in Fig. 12 are two images selected at 745 and 835 nm, and the corresponding co-registered image showing the percentage of oxygen saturation of the blood hemoglobin within the tumor area. We have adapted the model introduced in [35]–[37] and implemented in polar coordinates $(r, \theta)$, where $(r, \theta)$ are the point coordinates in the sample away from the ultrasound transducer. The oxygen saturation is computed with gradient descent parametric fitting totaling 14 measurements from 705 to 835 nm with about a 9-nm step. The model starts by defining the photoacoustic pressure $P(r, \theta, \lambda)$, at each point $(r, \theta)$ away from the array transducer center, after being detected by the system and spatially resolved by beamforming, as

$$P(r, \theta, \lambda) = C_0(r, \theta) F_0(\lambda) F(r, \theta, \lambda) \Gamma(r, \theta) \mu_a(r, \theta, \lambda),$$

where $\mu_a$ is the absorption coefficient at each point in the tissue (1/cm) for each wavelength $\lambda$, $F_0$ is the laser output energy per pulse (in joules) at each wavelength, $F$ is the normalized fluence distribution for each wavelength at each point in the imaging plane. $\Gamma$ is the dimensionless Grüneisen coefficient for each point in the tissue and $C_0$ is another normalization factor for each point $(r, \theta)$ in the imaging plane; which depends mainly on the photoacoustic impulse response of the tissue at each point $(r, \theta)$ convolved with the transducer impulse response and the temporal profile of the laser pulse [35]–[38]. $F(r, \theta, \lambda)$ can be approximated as wavelength-independent function $F(r, \theta)$ in the wavelength range from 705 to 835 nm, because the wavelength-dependent tissue scattering change in that window is small, and the wavelength-dependent absorption of the tissue is limited to small targets such as vessels, whereas most of the tissue has approximately the water absorption, which is almost constant over that wavelength window [35]–[40]. Hence, the normalized photoacoustic pressure by the laser energy per pulse $F_0(\lambda)$ can approximated as

$$P_{\text{normalized}}(r, \theta, \lambda) = C_0(r, \theta) F(r, \theta) \Gamma(r, \theta) \mu_a(r, \theta, \lambda)$$
$$P_{\text{normalized}}(r, \theta, \lambda) = C(r, \theta) \mu_a(r, \theta, \lambda),$$

where $C$ varies at every point in the sample but is independent of wavelength as long as the target is fixed with respect to the illumination and ultrasound detection. Therefore, for each point in our imaging plane $(r, \theta)$, we must solve a set of equations defined as

$$P_{\text{normalized}}(\lambda) = Wx,$$

$$\begin{bmatrix} P_{\text{normalized}}(\lambda_1) \\ P_{\text{normalized}}(\lambda_2) \\ P_{\text{normalized}}(\lambda_3) \\ \vdots \\ P_{\text{normalized}}(\lambda_n) \end{bmatrix} = \begin{bmatrix} \varepsilon_{\text{HBO}_2}(\lambda_1) & \varepsilon_{\text{HBr}}(\lambda_1) & 1 \\ \varepsilon_{\text{HBO}_2}(\lambda_2) & \varepsilon_{\text{HBr}}(\lambda_2) & 1 \\ \varepsilon_{\text{HBO}_2}(\lambda_3) & \varepsilon_{\text{HBr}}(\lambda_3) & 1 \\ \vdots & \vdots & \vdots \\ \varepsilon_{\text{HBO}_2}(\lambda_n) & \varepsilon_{\text{HBr}}(\lambda_n) & 1 \end{bmatrix} \begin{bmatrix} C[\text{HBO}_2] \\ C[\text{HBr}] \\ CK \end{bmatrix},$$

where $\varepsilon_{HBO_2}$ and $\varepsilon_{\text{HBr}}(\lambda)$ are the molar extinction coefficients of the oxy-hemoglobin and deoxy-hemoglobin as a function of the wavelength $\lambda$, respectively; both are tabulated in the literature for the wavelength range used [41]–[45]. [HBO$_2$] and [HBr] are the molar concentrations of the oxy-hemoglobin and deoxy-hemoglobin, respectively, which do not depend on wavelength. $K$ is the $y$-intercept, which represents the absorptions of water and other tissue constituents; all are assumed to be constant over the wavelength window used. The PAT RF data are averaged 7 times in this experiment for each frame over about 0.5 s, which is roughly proportional to the average optical absorption of the tissue over the cardiac cycle; hence, the computed oxygen saturation of the tissue should be related to the average oxygen saturation of the tissue at a given point in the imaging plane. Note that the points in the image with a PAT signal of less than 25 dB of the maximum were omitted from the computation process and thresholded out of the co-registered image.

The gradient descent optimization is for a least-squares error problem with a cost function ($J$) defined as the $l_2$-norm of error between the measurements and the model defined previously:

$$J = \| P_{\text{normalized}} (\lambda) - Wx \|^2.$$

The gradient is computed as

$$\nabla J = -2W^{\text{T}} \left( P_{\text{normalized}} (\lambda) - Wx \right).$$

The error minimization is carried out by the following gradient descent iterative equation:

$$x^{k+1} = x^k - \alpha \nabla J = x^k + 2\alpha W^{\text{T}} \left[ P_{\text{normalized}} (\lambda) - Wx \right],$$

where $x^{k+1}$ is the next iteration value of the $x$, $x^k$ is the previous iteration value of $x$, $\alpha$ is a constant that represents the optimization step size and controls the stability of the least-squares filter, and T indicates the matrix transposition operation [46]. The use of the least-square solution to find the best fit of oxygen saturation with measurements from multiple wavelengths was found to be more robust in estimating $sO_2$. After the optimization is finished, the oxygen saturation percentage ($sO_2$) can be computed as

$$sO_2 (r, \theta) = \frac{C(r,\theta)[\text{HBO}_2](r,\theta) \times 100\%}{C(r,\theta)[\text{HBO}_2](r,\theta) + C(r,\theta)[\text{HBr}](r,\theta)}$$
$$= \frac{[\text{HBO}_2](r,\theta) \times 100\%}{[\text{HBO}_2](r,\theta) + [\text{HBr}](r,\theta)}.$$

We can see that the spatially dependent constant is cancelled out and the $sO_2$ image can be constructed properly. The second supplementary video ( ) shows the progression of the fitted $sO_2$ image as we add more wavelength measurements. The first frame co-registered $sO_2$ image is computed from two wavelengths (745 and 835 nm) measurements only, and as the video continues, one more wavelength measurement is added to each frame from 705 until 835 nm. As shown in the movie, when the number of measurements increases, the $sO_2$ image is smoother. It is interesting to note that the $sO_2$ image calculated from 14-wavelength measurements (Fig. 12) shows higher oxygenation at the edge of the tumor compared with the level in the tumor core.

## V. Conclusion

Currently, we have four 16-channel modules plugged into the motherboard to form a 64-channel system. The achieved imaging speed in PE mode, PA mode, and co-registered mode are 1.5 frame/s, 5 frames/s and 1 frame/s respectively. The system hardware and FPGA parallel acquisition and processing design is capable of achieving video frame rate, but the slowest part in our current system is the DSP–PC link, which is a LAN interface of 1 Mbit/s. In the next prototype, we will incorporate an advanced DSP board with embedded FPGA and PCIe link of data transfer rate up to 1 Gbit/second, which will allow us to achieve up to 15 co-registered frames/second. The limitation in the co-registered imaging in that case will be the laser pulse repetition rate over the number of needed PA averages to achieve good signal-to-noise ratio.

In summary, we reported, to the best of our knowledge, a unique FPGA-based reconfigurable processor for real-time interlaced ultrasound and photoacoustic imaging. The system has a modular design which allows easy upgrading of the total number of channels. The processor features the ability to perform real-time switching between the two modalities by reconfiguring and adapting its structure with ultrafast speed, utilizing resources, and managing different I/Os; which hasn't been reported in the literature for these two modalities. Optional real-time acquisition of channel RF data is also featured by simply reprogramming the FPGAs with a slightly different code. Furthermore, a unique time-division multiplexing scheme is implemented to allow interlaced acquisition of ultrasound pulse-echo images without having to shut off the laser pulses. Several experiments were reported to demonstrate the *in vivo* imaging capability of the system and its potential application in imaging tumor vascular dynamics.

## Acknowledgments

## Biographies



**Umar Alqasemi** received a B.S. degree in electrical and computer engineering (biomedical engineering minor) from King Abdulaziz University, Jeddah, Saudi Arabia, in 2007, and an M.S. degree in biomedical engineering from the University of Connecticut (UConn), Storrs, CT, in 2011. He is currently a Ph.D. student in the Biomedical Engineering program at UConn with a full scholarship from King Abdulaziz University. He is working on the design and development of ultrasound and optical imaging systems and FPGA-based digital signal processing. He is a student member of the SPIE optical society and the vice president of the UConn SPIE student chapter.

**Hai Li** received his B.S. and M.S. degrees in biomedical engineering from Xi'an Jiaotong University at Shaanxi, China, in 2006 and 2009, respectively. He is a Ph.D. student in the Electrical and Computer Engineering Department of the University of Connecticut, Storrs, CT. He is working on the software design and implementation for ultrasound and photoacoustic imaging systems, digital signal processing, and simulations of photoacoustic imaging.



**Andrés Aguirre** received the B.S. degree in electronics engineering from Universidad Simón Bolívar, Sartenejas, Venezuela, in 1998 and the Ph.D. degree in biomedical engineering from the University of Connecticut, Storrs, CT, in 2010.

From 1998 to 2003, he worked in the cellular telephony field as an RF engineer, network engineer, and software developer. In 2005, he joined the Optical and Ultrasound Imaging Laboratory at the University of Connecticut, where he worked on the design and development of several diffuse optical tomography and photoacoustic imaging systems for breast and ovarian cancer detection. From 2006 to 2009, he was Treasurer of the UConn SPIE student chapter and President from 2009 to 2010. He is currently a product development engineer at CAS Medical Systems Inc. in Branford, CT.



**Quing (Ching) Zhu** received her Ph.D degree from the Bioengineering Department of the University of Pennsylvania in 1992 and she is currently a Professor in the Electrical and

Computer Engineering Department of the University of Connecticut. Professor Zhu's research has focused on the development of novel imaging devices combining ultrasound and diffused light, combining ultrasound and photoacoustic imaging, and combining nuclear detection and optical coherent tomography for breast and ovarian cancer detection and diagnosis. She has published more than 80 journal articles and numerous conference papers with her graduate students and postdoctoral fellows. She is a Fellow of SPIE, the International Society for Optics and Photonics, and serves as an editorial board member of *Biomedical Optics.*

## References

1. Wang LV. Ultrasound-mediated biophotonic imaging: A review of acousto-optical tomography and photoacoustic tomography. Dis Markers. 2003; 19(2–3):123–138. [PubMed: 15096709]

2. Prince, JL.; Links, JM. Medical Imaging Signals and Systems. Upper Saddle River, NJ: Pearson Prentice Hall; 2006. ch. 10 and 11

3. Emelianov SY, Aglyamov SR, Shah J, Sethuraman S, Scott WG, Schmitt R, Motamedi M, Karpiouk A, Oraevsky A. Combined ultrasound, optoacoustic and elasticity imaging. Proc SPIE. 2004; 5320:101–112.

4. Emelianov SY, Aglyamov SR, Karpiouk AB, Mallidi S, Park S, Sethuraman S, Shah J, Smalling RW, Rubin JM, Scott WG. Synergy and applications of combined ultrasound, elasticity, and photoacoustic imaging. IEEE Ultrasonics Symp. 2006:405–415.

5. Ermilov SA, Khamapirad T, Conjusteau A, Leonard MH, Lacewell R, Mehta K, Miller T, Oraevsky AA. Laser optoacoustic imaging system for detection of breast cancer. J Biomed Opt. Mar-Apr; 2009 14(2) art. no. 024007.

6. Aguirre A, Guo P, Gamelin J, Yan S, Sanders M, Brewer M, Zhu Q. Co-registered 3-D ultrasound and photoacoustic imaging system for ovarian tissue characterization. J Biomed Opt. 2009; 14(5) art. no. 054014.

7. Aguirre A, Ardeshirpour Y, Sanders M, Brewer M, Zhu Q. Potential role of co-registered photoacoustic and ultrasound imaging in ovarian cancer/detection and characterization. Transl Oncol. 2011; 4(1):29–37. [PubMed: 21286375]

8. Deán-Ben XL, Ntziachristos V, Razansky D. Statistical optoacoustic image reconstruction using a-priori knowledge on the location of acoustic distortions. Appl Phys Lett. Apr.2011 98(17) art. no. 171110.

9. Modgil D, La Rivière PJ. Image reconstruction in photoacoustic tomography with variable speed of sound using a higher-order geometrical acoustics approximation. J Biomed Opt. Mar.2010 15(2) art. no. 021308.

10. Cox BT, Kara S, Arridge SR, Beard PC. k-Space propagation models for acoustically heterogeneous media: Application to biomedical photoacoustics. J Acoust Soc Am. 2007; 121(6): 3453–3464. [PubMed: 17552697]

11. Niederhauser JJ, Jaeger M, Lemor R, Weber P, Frenz M. Combined ultrasound and optoacoustic system for real-time high-contrast vascular imaging in vivo. IEEE Trans Med Imaging. Apr; 2005 24(4):436–440. [PubMed: 15822801]

12. Sethuraman S, Aglyamov SR, Amirian JH, Smalling RW, Emelianov SY. Development of a combined intravascular ultrasound and photoacoustic imaging system. Proc SPIE Photonics West. 2006; 6086:F1–F10.

13. Guo P, Gamelin J, Yan S, Aguirre A, Zhu Q. Co-registered 3-D ultrasound and photoacoustic imaging using a 1.75D 1280-channel ultrasound system. Proc SPIE. 2007; 6437 art. no. 643713.

14. Kolkman RGM, Brands PJ, Steenbergen W, van Leeuwen TG. Real-time in vivo photoacoustic and ultrasound imaging. J Biomed Opt. Sep-Oct;2008 13(5) art. no. 050510.

15. Ermilov SA, Fronheiser MP, Brecht H-P, Su R, Conjusteau A, Mehta K, Otto P, Oraevsky AA. Development of laser optoacoustic and ultrasonic imaging system for breast cancer utilizing handheld array probes. Proc SPIE. 2009; 7177 art. no. 717703.

16. Harrison T, Ranasinghesagara JC, Lu H, Mathewson K, Walsh A, Zemp RJ. Combined photoacoustic and ultrasound biomicroscopy. Opt Express. Nov; 2009 17(24):22041–22046. [PubMed: 19997449]

17. Hu C-H, Xu X-C, Cannata JM, Yen JT, Shung KK. Development of a real-time, high-frequency ultrasound digital beamformer for high-frequency linear array transducers. IEEE Trans Ultrason Ferroelectr Freq Control. 2006; 53(2):317–323. [PubMed: 16529106]

18. Tsang IKH, Yiu BYS, Cheung DKH, Chiu HCT, Cheung CCP, Yu ACH. Design of a multi-channel pre-beamform data acquisition system for an ultrasound research scanner. Proc IEEE Int Ultrasonics Symp. 2009:1840–1843.

19. Hauck, S.; DeHon, A. Reconfigurable Computing: The Theory and Practice of FPGA-Based Computation. Amsterdam, The Netherlands: Elsevier; 2008.

20. Octal LNA/VGA/AAF/ADC and Crosspoint Switch: AD9272. Analog Devices, Inc.; Norwood, MA: 2007. Rev. C

21. Evaluating the AD9272/AD9273 for Ultrasound Systems: Evaluation Board User Guide. Analog Devices, Inc.; Norwood, MA: 2009. UG001, Rev. 0

22. High Speed Converter Evaluation Platform: HSC-ADC-EVALC. Analog Devices, Inc.; Norwood, MA: 2007. Rev. 0

23. Gamelin J, Maurudis A, Aguirre A, Huang F, Guo P, Wang LV, Zhu Q. A real-time photoacoustic tomography system for small animals. Opt Express. 2009; 17(13):10489–10498. [PubMed: 19550444]

24. Gamelin J, Aguirre A, Maurudis A, Huang F, Castillo D, Wang LV, Zhu Q. Curved array photoacoustic tomographic system for small animal imaging. J Biomed Opt. May-Jun;2008 13(2) art. no. 024007.

25. Guo, P. Ph D dissertation. Dept Electrical and Computer Engineering, University of Connecticut; Storrs, CT: 2007. Three dimensional ultrasound imaging and its application in combined near-infrared optical imaging and co-registered photoacoustic imaging; p. 1-3.

26. Roth, C., Jr; Kinney, LL. Fundamentals of Logic Design. 6th. Independence, KY: CENGAGE Learning; 2010.

27. Chang, KC. Digital Systems Design With VHDL and Synthesis: An Integrated Approach. New York, NY: Wiley-IEEE Computer Society Press; 1999.

28. D'Hollander, E.; Joubert, GR.; Peters, F.; Trottenberg, U. Parallel Computing: Fundamentals, Applications, and New Directions. Amsterdam, The Netherlands: Elsevier Science; 1998.

29. TMS320C6455 DSK Technical Reference. Spectrum Digital Inc.; Stafford, TX: 2006. Rev. C

30. Maichen, W. Digital Timing Measurements: From Scopes and Probes to Timing and Jitter. New York, NY: Springer; 2006.

31. Virtex-4 FPGA User Guide. Xilinx Inc.; San Jose, CA: Dec 1. 2008 UG070 (v2.6)

32. Gautschi, W. Numerical Analysis: An Introduction. Cambridge, MA: Birkhauser Boston; 1997. ch. 2

33. Chen NG, Guo PY, Yan SK, Piao DQ, Zhu Q. Simultaneous near infrared diffusive light and ultrasound imaging. Appl Opt. Dec; 2001 40(34):6367–6380. [PubMed: 18364946]

34. Biswal NC, Pavlik C, Smith MB, Aguirre A, Xu Y, Zanganeh S, Kuhn LT, Claffey KP, Zhu Q. Imaging tumor hypoxia by near infrared fluorescence tomography. J Biomed Opt. Jun.2011 16 art. no. 066009.

35. Laufer J, Elwell C, Delpy D, Beard P. In vitro measurements of absolute blood oxygen saturation using pulsed near-infrared photoacoustic spectroscopy: Accuracy and resolution. Phys Med Biol. 2005; 50(18):4409–4428. [PubMed: 16148401]

36. Wang X, Pang Y, Ku G, Xie X, Stoica G, Wang LV. Noninvasive laser-induced photoacoustic tomography for structural and functional *in vivo* imaging of the brain. Nat Biotechnol. Jul; 2003 21(7):803–806. [PubMed: 12808463]

37. Wang LV, Wang X, Ku G, Xie X, Stoica G. High-resolution spectroscopic photoacoustic tomography for non-invasive functional imaging of small-animal brains in vivo. Second Asian and Pacific Rim Symp Biophotonics. 2004:246–247.

38. Wang X, Xie X, Ku G, Wang LV, Stoica G. Noninvasive imaging of hemoglobin concentration and oxygenation in the rat brain using high-resolution photoacoustic tomography. J Biomed Opt. May. 2006 11 art. no. 024015.

39. Wang, LV.; Wu, H. Biomedical Optics: Principles and Imaging. New York, NY: Wiley; 2007. ch. 12

40. Tuchin, V.; Optics, T. Light Scattering Methods and Instruments for Medical Diagnosis. 2nd. Bellingham, WA: SPIE Press; 2000.

41. Horecker BL. The absorption spectra of hemoglobin and its derivatives in the visible and near infrared regions. J Biol Chem. 1943; 148(1):173–183.

42. van Kampen EJ, Zijlstra WG. Determination of hemoglobin and its derivatives. Adv Clin Chem. 1965; 8:141–187. [PubMed: 5321443]

43. Zijlstra WG, Buursma A, Zwart A. Molar absorptivities of human hemoglobin in the visible spectral range. J Appl Physiol. 1983; 54(5):1287–1291. [PubMed: 6863089]

44. Cordone L, Cupane A, Leone M, Vitrano E. Optical absorption spectra of deoxy- and oxyhemoglobin in the temperature range 300–20 K. Biophys Chem. 1986; 24(3):259–275. [PubMed: 3768470]

45. Kim JG, Xia M, Liu H. Extinction coefficients of hemoglobin for near-infrared spectroscopy of tissue. IEEE Eng Med Biol Mag. 2005; 24(2):118–121. [PubMed: 15825855]

46. Bar-Shalom, Y.; Li, XR.; Kirubarajan, T. Estimation with Applications to Tracking and Navigation. New York, NY: Wiley; 2001.
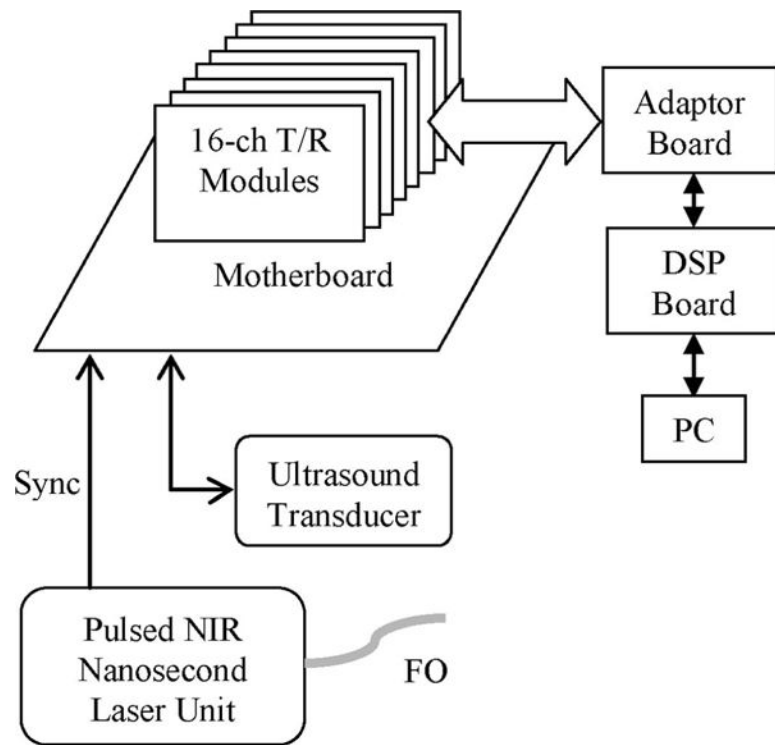
**Fig. 1.**
The overall block diagram of co-registered imaging system.
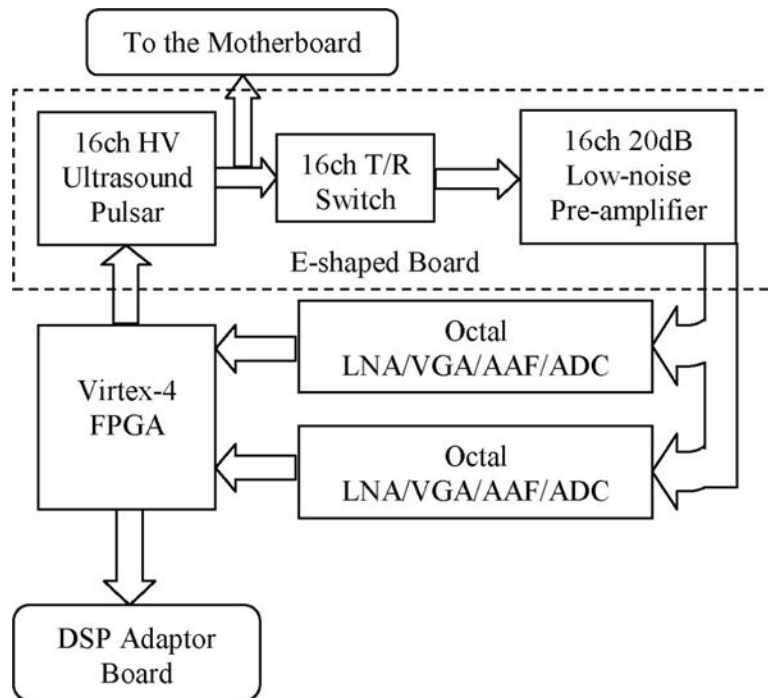
**Fig. 2.**
The block diagram of one 16-channel module.
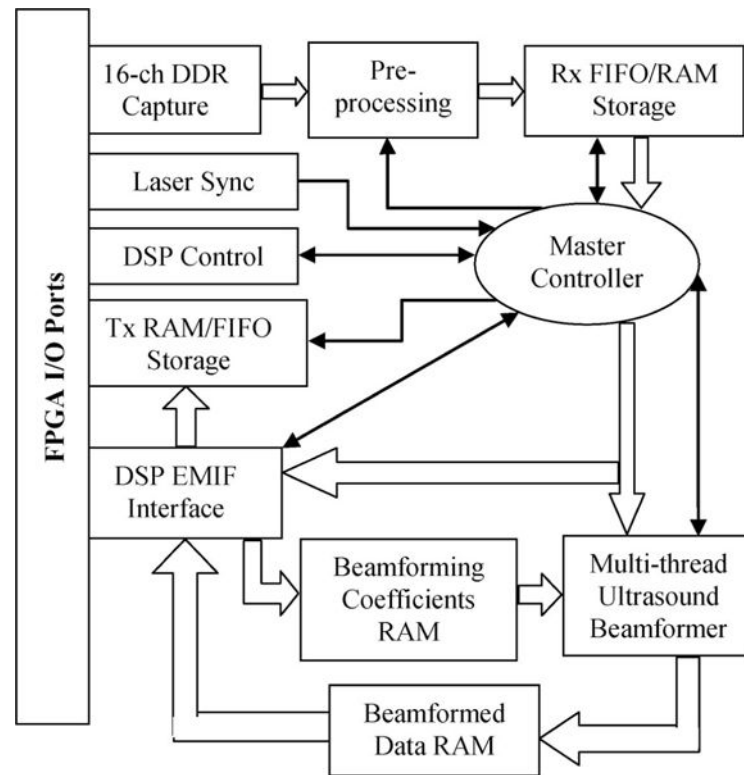
**Fig. 3.**
The overall block diagram of the field-programmable gate array (FPGA) code.
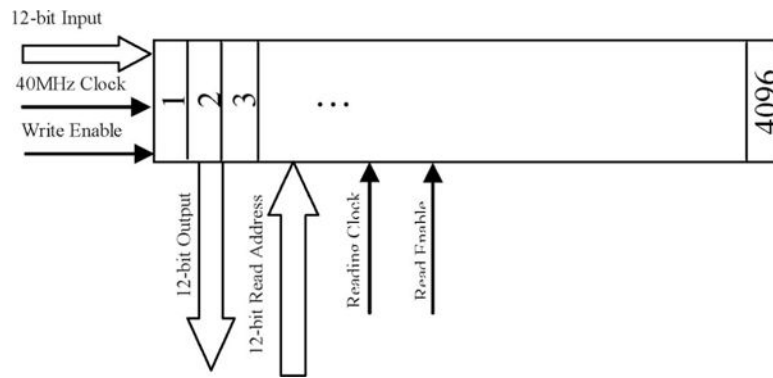
**Fig. 4.**
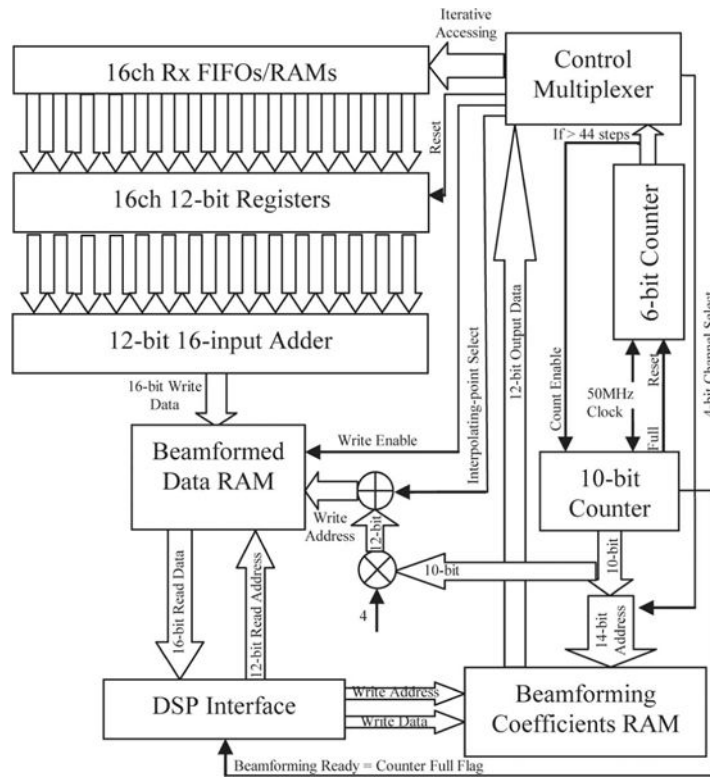The block diagram of the receive (Rx) first-in, first-out (FIFO)/RAM.

**Fig. 5.**
The block diagram of the beamforming code.
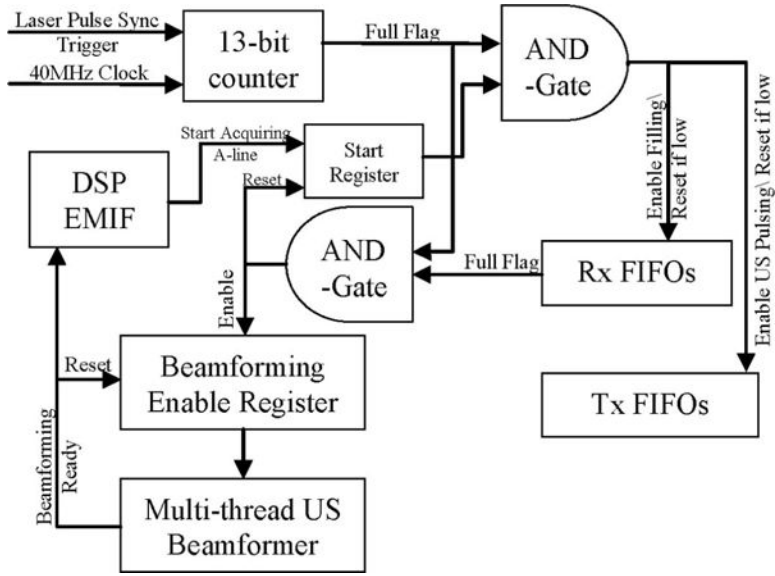
**Fig. 6.**
Block diagram of the time-division multiplexing (TDM) scheme for acquiring the pulse-echo (PE) A-lines while the laser is pulsing to ensure no photoacoustic (PA) interference. Note that the 12-bit counter starts counting when it is triggered by the laser synchronizing pulse until it is full, then it waits until the next laser pulse, when it resets and starts counting again.
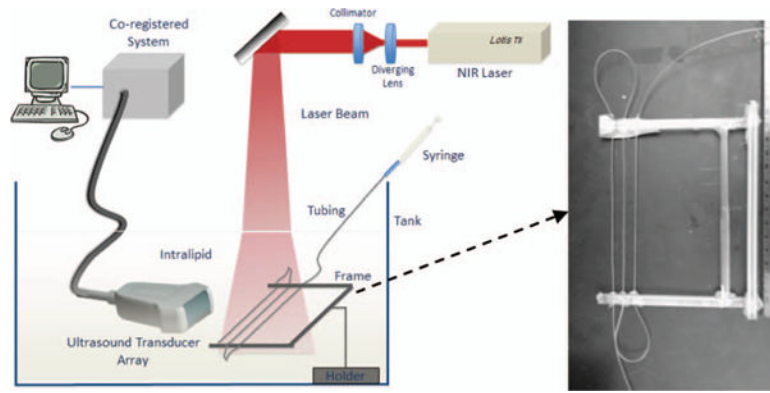
**Fig. 7.**
(left) The phantom experiment setup and (right) a photograph of the tubing phantom used.
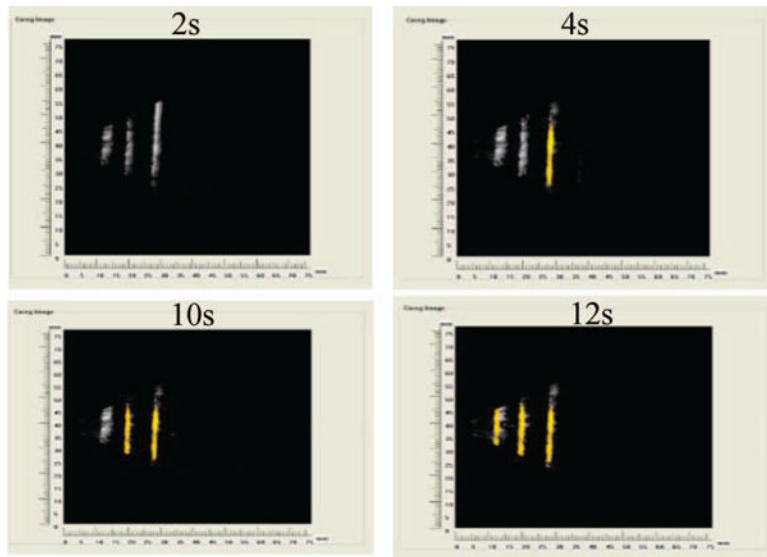
**Fig. 8.**
The dynamics of filling the tubing phantom with ink.
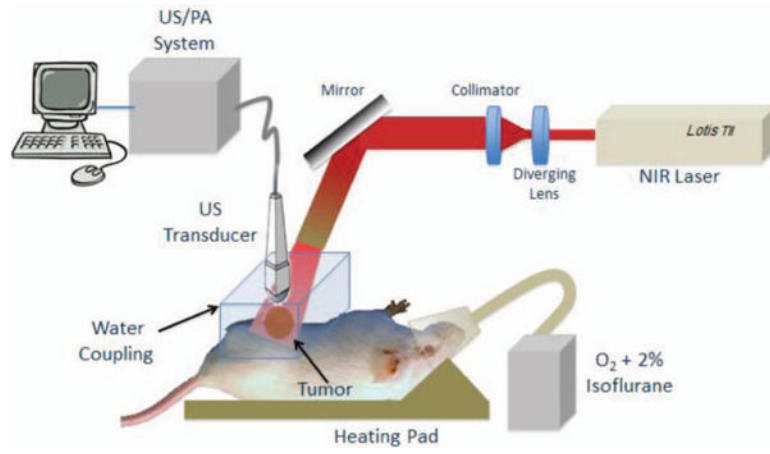
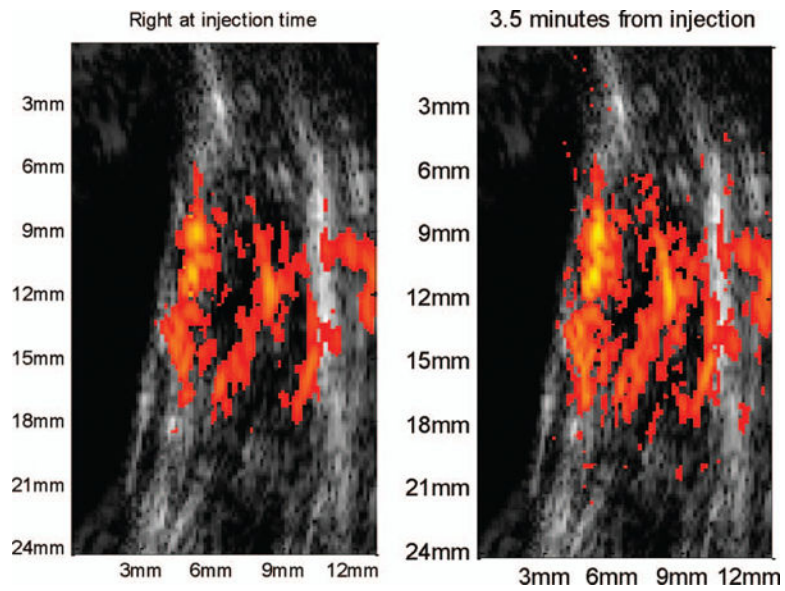**Fig. 9.**
Mouse experiment setup.

**Fig. 10.**
(left) The co-registered images at injection time, and (right) 3.5 minutes after injection; the photoacoustic tomography (PAT) parts of the images were normalized to the same value with 20 dB dynamic range.
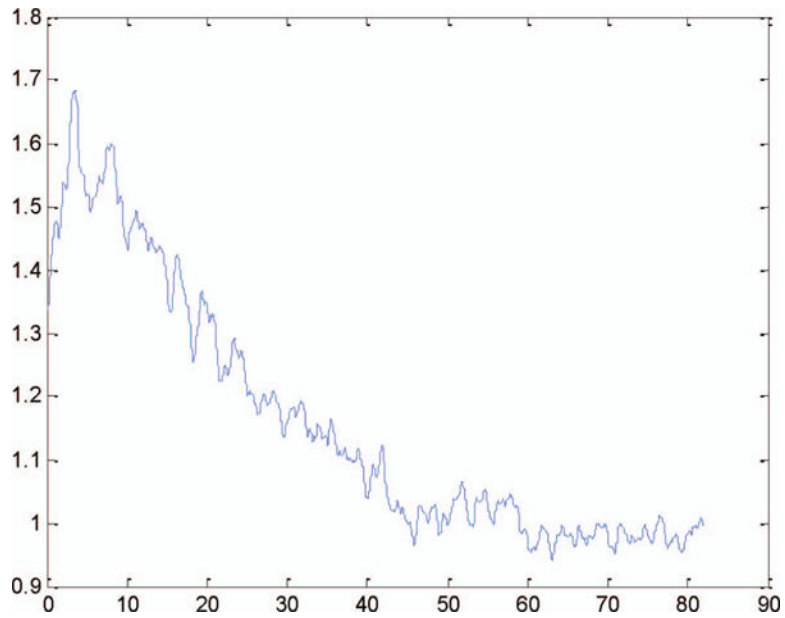
**Fig. 11.**
The maximum photoacoustic signal in tumor area right after injection of indocyanine green (ICG) of 100 μM concentration, normalized to the maximum photoacoustic signal at the time of injection.
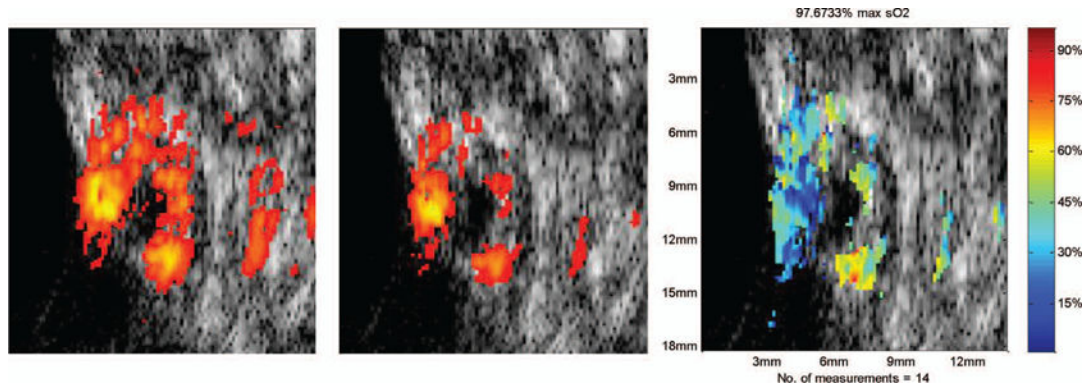
**Fig. 12.**
Co-registered photoacoustic tomography (PAT) images selected at (left) ~745 nm, and (middle) ~835 nm, showing different light absorption distributions over the tumor area. (right) The co-registered oxygen saturation image shows higher blood oxygen saturation at the edge compared to the core area. The actual image size is $1.8 \times 1.35$ cm.